JACS
JOURNAL OF THE AMERICAN CHEMICAL SOCIETY

ARTICLE

pubs.acs.org/JACS

Electronic Structure Description of a $[Co(III)_3Co(IV)O_4]$ Cluster: A Model for the Paramagnetic Intermediate in Cobalt-Catalyzed Water Oxidation

J. Gregory McAlpin,[†] Troy A. Stich,[†] C. André Ohlin,[†,⊥,‡] Yogesh Surendranath,[§,∥] Daniel G. Nocera,[§] William H. Casey,[†,‡] and R. David Britt*[,†]

[†]Department of Chemistry and [‡]Department of Geology, University of California, One Shields Avenue, Davis, California 95616, United States

[⊥]School of Chemistry, Monash University, Vic 3800, Australia

[§]Department of Chemistry, Massachusetts Institute of Technology, 77 Massachusetts Avenue, Cambridge, Massachusetts 02139, United States

Supporting Information

ABSTRACT: Multifrequency electron paramagnetic resonance (EPR) spectroscopy and electronic structure calculations were performed on $[Co_4O_4(C_5H_5N)_4(CH_3CO_2)_4]^+$ ($\mathbf{1}^+$), a cobalt tetramer with total electron spin $S = 1/2$ and formal cobalt oxidation states III, III, III, and IV. The cuboidal arrangement of its cobalt and oxygen atoms is similar to that of proposed structures for the molecular cobaltate clusters of the cobalt−phosphate (Co−Pi) water-oxidizing catalyst. The Davies electron−nuclear double resonance (ENDOR) spectrum is well-modeled using a single class of hyperfine-coupled ^{59}Co nuclei with a modestly strong interaction (principal elements of the hyperfine tensor are equal to $[-20(\pm2), 77(\pm1), -5(\pm15)]$ MHz). Mims ^{1}H ENDOR spectra of $\mathbf{1}^+$ with selectively deuterated pyridine ligands confirm that the amount of unpaired spin on the cobalt-bonding partner is significantly reduced from unity. Multifrequency ^{14}N ESEEM spectra (acquired at 9.5 and 34.0 GHz) indicate that four nearly equivalent nitrogen nuclei are coupled to the electron spin. Cumulatively, our EPR spectroscopic findings indicate that the unpaired spin is delocalized almost equally across the eight core atoms, a finding corroborated by results from DFT calculations. Each octahedrally coordinated cobalt ion is forced into a low-spin electron configuration by the anionic oxo and carboxylato ligands, and a fractional electron hole is localized on each metal center in a Co $3d_{xz,yz}$-based molecular orbital for this essentially $[Co^{+3.125}{}_4O_4]$ system. Comparing the EPR spectrum of $\mathbf{1}^+$ with that of the catalyst film allows us to draw conclusions about the electronic structure of this water-oxidation catalyst.

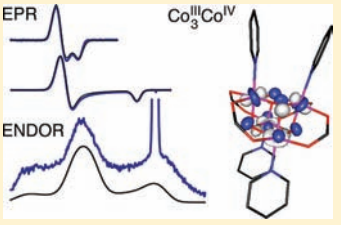

INTRODUCTION

A cobalt−phosphate (Co−Pi) catalyst can perform the demanding reaction of water oxidation under mild conditions (neutral pH and in aqueous solution).[1] At low overpotential, the catalyst is able to self-assemble into an amorphous film on the electrode surface,[1,2] self-repair,[3] and oxidize water in a variety of different buffered solutions.[4,5] Another attribute is that it is composed of relatively low-cost inorganic precursors.[6]

The catalyst film forms as aqueous Co(II) is oxidized to Co(III) and deposits onto the electrode surface.[7] Anodic waves from cyclic voltammetry studies indicate a $Co^{2+/3+}$ couple (1.13 V vs standard hydrogen electrode, SHE) prior to the catalytic water oxidation wave.[5,8] Just one monolayer of this cobalt-oxide on the electrode surface is sufficient for catalysis, even if, after the initial assembly, the electrode is put into cobalt-free buffer. If the Co−Pi catalyst layer is removed from the electrode surface and the electrode is placed in cobalt-free buffer, no water oxidation is observed.

Two independent X-ray absorption spectroscopic (XAS) studies have been conducted to elucidate the structure of the amorphous water-oxidizing film.[9,10] These studies found that the film was composed of discrete molecular units, as opposed to a mineral-like continuous extended structure. Both studies rationalized the extended X-ray absorption fine structure (EXAFS) portion of the XAS spectrum by invoking a multicobalt oxo-bridged core for the catalyst. Dau and co-workers studied the film shortly after it was removed from oxidizing potential and suggested that it was composed of clusters of complete and incomplete vertex-sharing cobalt-oxo cubanes (Figure 1b). Nocera, Yachandra, and co-workers measured the XAS spectrum in situ, while the film was under potential, and favored a core of edge-sharing CoO_6 octahedra (Figure 1a). This latter arrangement is reminiscent of the structural motif present in brucite-like double-hydroxide layers differing only in that it lacks a complete cubane motif.

In the mechanism we have proposed, two closely associated Co(IV) moieties oxidize two water molecules by four electrons and mediate O−O bond formation.[2,8,11] The liberated protons from the reaction are taken up by the buffering agent. Continuous-wave

Received: March 14, 2011
Published: September 13, 2011

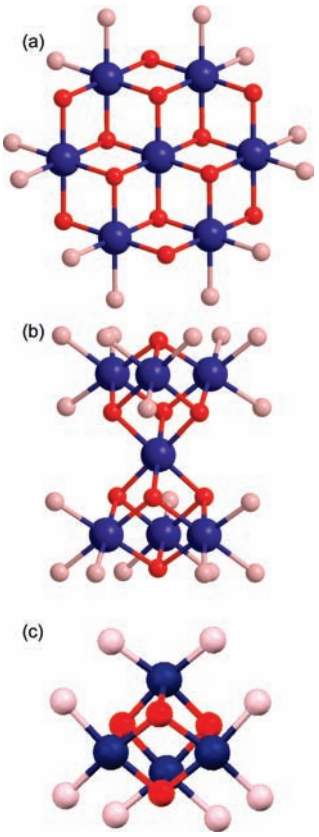

Figure 1. Proposed structural models based on XAS experiments performed (a) by Nocera, Yachandra, and co-workers during catalytic turnover and (b) by Dau and co-workers after the oxidizing potential is removed. Cuboidal "core" of $\mathbf{1}^+$ (c). Cobalt nuclei (blue), bridging oxygens (red), and terminal oxygens (pink).

electron paramagnetic resonance (CW EPR) spectroscopic studies support this claim.[12] At pH 7, only when potentials applied are sufficient for water oxidation does an EPR signal appear that is tentatively assigned to an $S = 1/2$ d^5 Co(IV)-containing species. This assignment was based partly on the similarity of the EPR spectrum to that of $[Co_4O_4(C_5H_5N)_4(CH_3CO_2)_4]^+$ ($\mathbf{1}^+$) with formal cobalt oxidation states of (III, III, III, and IV). The crystal structure of the all-cobaltic form ($\mathbf{1}^0$) shows it to be an oxo-bridged cobalt cubane (Scheme 1).

While several mineral-based Co(IV)-containing systems have been studied,[13−20] only a few examples of structurally and spectroscopically well-characterized, stable, molecular cobalt complexes with a Co(IV) oxidation state exist (Table 1). In addition to $\mathbf{1}^+$, only one other cuboidal cobalt complex with a stable Co(IV) oxidation state is known.[21] Notably, this complex has been used to model proton-coupled electron transfer self-exchange reactions believed to facilitate electron hopping through the amorphous catalyst films.[22] Modeling the electronic/geometric structure relationships of such multinuclear cobalt clusters is a critical first step to our understanding of the factors that drive water oxidation in the Co−Pi film.

Here we compare the electronic structure properties of $\mathbf{1}^+$ to those for the paramagnetic intermediate found during water oxidation by Co−Pi. The magnetic parameters determined by electron nuclear double resonance (ENDOR) and electron spin echo envelope modulation (ESEEM) spectroscopic results combined with results from density functional theory (DFT) calculations reveal that

Scheme 1. Schematic Representation of $[Co_4O_4(C_5H_5N)_4(CH_3CO_2)_4]^{+/0}$ ($\mathbf{1}^{+/0}$)

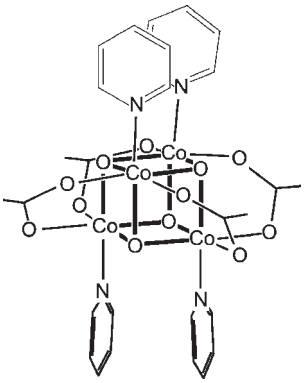

the unpaired spin of $\mathbf{1}^+$ is highly delocalized. Each octahedrally coordinated cobalt ion is forced into a low-spin electron configuration by the anionic oxo and carboxylato ligands, and a fractional electron hole resides on each metal center in a Co $3d_{xz,yz}$-based molecular orbital. These results are compared to what is known of the electronic structure of the putative Co(IV) intermediate in Co−Pi and allow us to evaluate the proposed structures of Co−Pi based on the XAS results.[9,10]

MATERIALS AND METHODS

Synthesis. $[Co_4O_4(C_5H_5N)_4(CH_3CO_2)_4](ClO_4)$ ($\mathbf{1}^0$) was synthesized following the literature procedure.[23] Anhydrous sodium acetate (1.64 g) was dissolved in water (7 mL) and added to a solution of cobalt(II) nitrate hexahydrate (2.9 g) in methanol (30 mL) at room temperature. Upon addition, the solution changed color from pink to violet. The solution was then heated, and pyridine (0.8 mL) was added when the solution reached 70 °C, followed by dropwise addition of hydrogen peroxide (30%, 5 mL). This led to an immediate color change to dark green. The solution was refluxed for 4 h and then allowed to cool.

Dichloromethane (100 mL) was added, and both phases were vigorously mixed. The dichloromethane was separated from the aqueous phase, which was pinkish, and discarded. The dichloromethane phase was placed in an uncovered crystallization dish, and the solvent was allowed to evaporate, yielding 1.7 g of crude product. The product was redissolved in 9 mL of dichloromethane in a 15 mL tube, and 2 mL of water was added. The tube was capped and shaken, followed by careful removal of the upper 2 mL. The darkness of both phases made it difficult to tell where the phase meniscus was located, which is why a volumetric pipet was employed to remove the aqueous phase. Anhydrous sodium sulfate (2 g) was added, and the mixture was shaken and then filtered through a Pasteur pipet filled with glass wool. The first water fraction was discarded, and the wool was washed with dichloromethane. Crystals of the product and residual sodium sulfate were obtained by the next day. The product was dissolved in dichloromethane, filtered, and allowed to evaporate to yield the pure product ($\mathbf{1}^0$).

Electrochemical oxidation of $\mathbf{1}^0$ was performed with a Princeton Applied Research model 263A potentiostat and PowerStep software package using the previously published procedures.[12] A potential of up to 1.1 V relative to a Ag^0 pseudoreference electrode was applied to a 5 mM solution of $\mathbf{1}^0$ in CH_3CN in the presence of 0.4 M $LiClO_4$. The potential was applied until the current density reached a steady state. The total number of liberated electrons measured was less than one equivalent of the amount of $\mathbf{1}^0$ present in solution (≈0.5 charge equivalents), suggesting that each molecule was oxidized by, at most, one

Table 1. EPR Parameters of Other Co(IV) Complexes[a]

compound	g1	g2	g3	$A(^{59}Co)$ MHz			Reference
(OEC)Co(C_6H_5)	1.97	2.11	2.00	72	8	10	34
[(OMTPC)Co(PPH_3)]$^+$	2.14	2.00	1.89				35
[Co(S_2CNc-Hx_2)$_3$]$^+$	2.65	2.65	1.90				52
Co(η^4-**1**)	2.56	2.17	2.02	42			53
Co(η^4-**2**)	2.57	2.17	2.02	53			53
Co(η^4-**3**)	2.57	2.19	2.02	53			53
(CH_3)Co(dpgH)$_2^+$	2.026	2.026	2.025	14	14	87	54
(CH_3CH_2)Co(dmgH)$_2^+$	2.029	2.029	2.031	13	13	94	54
(CH_3)Co(4-MeO-dpgH)$_2^+$	2.026	2.026	2.027	13	13	81	55
(*n*-butyl)CoSalen$^+$	2.21	2.09	1.99	202	112	76	56
CoO_2	2.03	2.03	2.00	2553	2553	3150	19
$(Sr_{0.5})(La_{1.5})Li_{0.5}Co_{0.5}O_4$	2.55		>0.85				13
	−2.32						
Al_2O_3: Co,Mg	2.58			300			18
$(La_{2-X})(Sr_X)Li_{0.5}(Co_{0.5})O_4$	2.44	2.24	~0.8	321	<30	~90	20
$[Co_4O_4(OAc)_2(bpy)_2]^{3+}$	2.20						21
$[Co_4O_4(OAc)_4(py)_4]ClO_4$	2.35	2.32	2.06	−20	77	−5	this work

[a] OEC is 2,3,7,8,12,13,17,18-octaethylcorrole. OMTPC is 5,10,15-tri-phenyl-2,3,7,8,12,13,17,18-octamethylcorrolato. (S_2CNc-Hx_2)$_3$ is tris-(dithiocarbamato cyclohexyl). (η^4-**1**) is 5,6-(4,5-dichlorobenzo)-3,8,11,13-tetraoxo-2,2,9,9-tetramethyl-12,12-diethyl-1,4,7,10-tetraazacyclotridecan. (η^4-**2**) is 5,6-benzo-3,8,11,13-tetraoxo-2,2,9,9-tetramethyl-l2,12-diethyl-1,4,7,10-tetraazacyclotridecane. (η^4-**3**) is 5,6-(43-dimethoxybenzo)-3,8,11,13-tetraoxo-2,2,9,9-tetramethyl-12,12-diethyl-1,4,7,10-tetraazacyclotridecane. dpgH is diphenylglyoxime. dmgH is dimethylglyoxime. MeO-dpgH is MeO-DPH2 = -4,4^1 -dimethoxydiphenylglyoxime. Salen is bis (salicylidenato)ethylenediamine. bpy is bipyridine. py is pyridine.

electron. The solution was reduced to approximately one-fifth the original volume, titurated with water (20 mL), and refrigerated overnight to facilitate crystal growth. An approximately 15% yield of **1**$^+$ was obtained. Isolated crystals were washed with water and redissolved in a 1:1 mixture of acetonitrile and dichloromethane. Solutions were sealed under air in 3 mm and 1.2 mm OD quartz tubes for X-band and Q-band EPR study, respectively. These samples were then stored in liquid nitrogen.

Spectroscopy. X-band CW EPR spectra were recorded using a Bruker (Billerica, MA) ECS106 spectrometer equipped with a TE_{102} resonator (ER4102ST). Cryogenic temperatures were achieved and controlled using an Oxford Instruments ESR900 liquid helium cryostat in conjunction with an Oxford Instruments ITC503 temperature and gas flow controller. All CW EPR data were acquired under nonsaturating, slow-passage conditions.

Electron spin−echo (ESE) detected EPR ($\pi/2$-τ-π-τ-echo), three-pulse ESEEM ($\pi/2$-τ-$\pi/2$-T-$\pi/2$-τ-echo), and Davies ENDOR (π-RF-$\pi/2$-τ-π-τ-echo) experiments were performed using a Bruker E-580 EleXsys spectrometer. Studies at X-band excitation frequencies (ca. 9.5 GHz) were carried out in a cylindrical dielectric cavity (MD5, Bruker). CW and pulse Q-band studies (ca. 34 GHz) were done using a laboratory-built probe[24,25] modified to fit into an Oxford 935CF cryostat. All simulations were performed using the EasySpin 3.1.5 toolbox[26,27] in MatLab (The Mathworks Inc., Natick, MA).

Density Functional Theory Computations. All DFT calculations were performed on a cluster of AMD Dual Opteron processors (PSSC Laboratories) running the Red Hat Enterprise Linux 4.5 operating system using the ORCA 2.6.35 suite of software.[28] The starting geometry for each computational model was based on the X-ray crystal structure coordinates of **1**^{0} (CSD accession code QIVQIW).[23] The β-methyl group on each of the four acetate ligands was replaced by a hydrogen atom to aid in computational convergence. Two models of **1**$^+$ were generated: one (MOD-**1**$^+$xtal) that used the X-ray coordinates of **1**^{0} with one electron removed and only the positions of the H atoms were optimized, and one (MOD-**1**$^+$opt) wherein the positions of all atoms were optimized. Unrestricted Kohn−Sham geometry optimizations were carried out using the Perdew−Wang 91 (PW91) local density and Perdew−Burke−Ernzerhof (PBE) generalized gradient functionals[29] with the TZVP (Ahlrichs polarized triple-ζ valence)

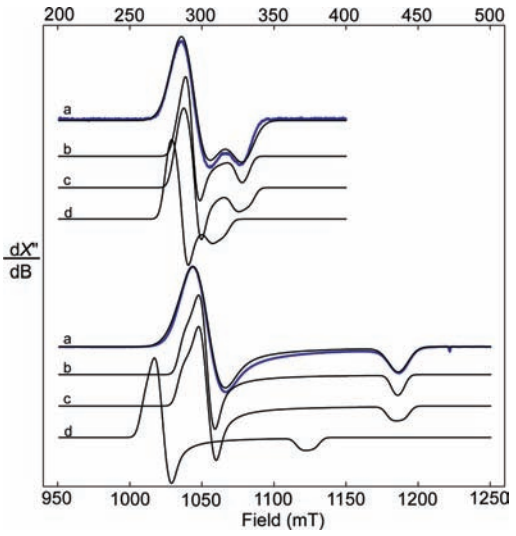

Figure 2. X- and Q-band CW spectra of **1**$^+$ (blue). Simulations were performed by fitting both spectral frequencies simultaneously with g = [2.35, 2.32, 2.06] and unresolved hyperfine coupling. X-band H Strain = [682 638 435] MHz; Q-band H Strain = [790, 630, 430] MHz (black, a). Simulations were also performed using the best-fit g-values above, $A(^{59}Co)$ values obtained by simulation of Davies ENDOR, and DFT calculated (MOD-**1**$^+$xtal) orientations (b), using the best-fit g-values above with the four DFT calculated $A(^{59}Co)$ values and tensor orientations (c), and DFT calculated g-values, $A(^{59}Co)$ values, and hyperfine orientations (gray, d). Spectrometer settings: temperature = 10 K; X-band microwave power = 1.02 mW; Q-band microwave power = 1.92 mW.

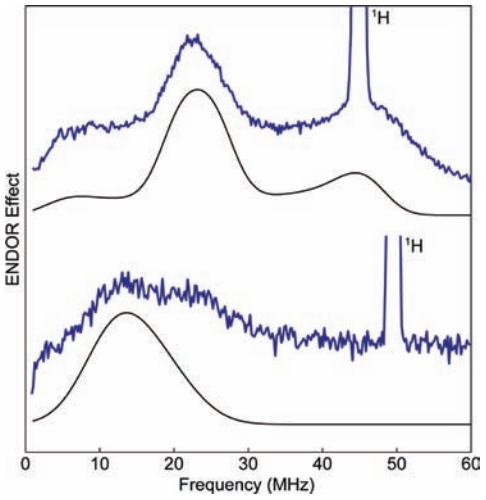

Figure 3. Davies ENDOR of $\mathbf{1}^+$ (blue) acquired at B_0 = 1053 mT (top) and 1165 mT (bottom) and corresponding simulations (black) that achieved using two classes of two ^{59}Co centers: $A(^{59}\text{Co})$ = [−20, 76, 5] MHz and [76, −20, 5] MHz. Spectrometer settings: $t_{\pi/2}$ = 124 ns; τ = 500 ns; RF pulse length = 25 μs; temperature = 10 K.

basis set on the four cobalt ions and the SVP (Ahlrichs polarized split valence)[30] basis on all other atoms. Geometry optimizations used the following convergence criteria: $5E^{-06}$ Hartree change in total energy, $3E^{-04}$ Hartree/Bohr change in the Cartesian gradient, and $4E^{-03}$ Bohr change in the Cartesian coordinates between successive cycles.

Single-point calculations on the converged geometries were performed with the hybrid functional PBE0. The following basis sets were employed: core properties basis with triple polarization (CP(PPP)) on Co, TZVP on all N and O atoms, and SVP on C and H atoms. EPR properties were computed using coupled-perturbed self-consistent field (CP-SCF) theory with the origin of the gauge-dependence set at the center of electronic charge.[31] Isosurface plots of the molecular orbitals were generated with the gOpenmol program using an isodensity value of 0.06 au.[5,32]

RESULTS

Electron Paramagnetic Resonance. The X- and Q-band CW EPR spectra of $\mathbf{1}^+$ exhibit an approximately axial line shape (Figure 2) with apparent g-values of $g_\perp$ = 2.33 and $g_{||}$ = 2.06. No features at lower field are apparent that would indicate the presence of an intermediate (S = 3/2)[33] or high-spin species (S = 5/2). We model the spectra as arising from a low-spin, S = 1/2, system with g-values =2.35, 2.32, and 2.06 determined by simultaneous least-squares fitting of data acquired at both frequencies. The formulation of this species as containing a single unpaired electron is supported by room-temperature solid-state magnetic susceptibility studies on the bipyridine analogue of $\mathbf{1}^+$.[21] The measured effective magnetic moment of only 2.2 Bohr magnetons indicated that there are no higher spin states populated at these relatively high temperatures. No hyperfine interactions (HFI) are apparent for any of the magnetic nuclei present in the complex (^{59}Co, ^{14}N, ^{1}H). For example, if the single unpaired electron were localized on a single ^{59}Co center (I = 7/2), eight EPR transitions and a large metal HFI value would be expected. While such hyperfine interactions tend to result in easily resolved splittings, there are several examples of cobalt species without such a structure in the EPR spectrum.[34,35]

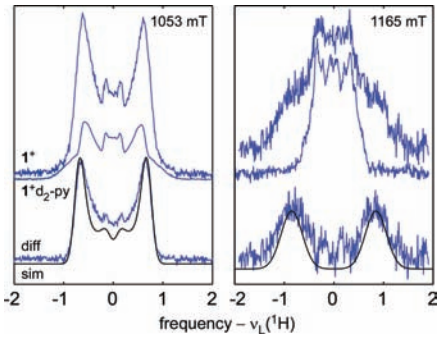

Figure 4. Q-band Mims ENDOR spectra of $\mathbf{1}^+$, $\mathbf{1}^+$ d_2-py, and the corresponding difference spectrum collected at 1053 mT (left panel) and 1165 mT (right panel). Simulations (black traces) include one class of protons with hyperfine $A(^1\text{H})$ = [0.45, 1.45, −1.90] MHz. Spectrometer settings: temperature = 10 K; $t_{\pi/2}$ = 32 ns; τ = 188 ns (for B_0 = 1053 mT data) and τ = 228 ns (for B_0 = 1165 mT data); RF pulse length = 16 μs.

Alternatively, if the unpaired electron was delocalized over all four ^{59}Co centers of $\mathbf{1}^+$, 4096 ($(2I + 1)^n$, n = number of nuclei) transitions would be expected. With such a large number of overlapping transitions, it is easy to imagine how ^{59}Co structural features could be lost in the inhomogeneously broadened EPR spectrum. To model the spectral line width at g = 2.36, 2.32, and 2.06, an anisotropic, unresolved hyperfine interaction of [790, 630, and 430] MHz was used in the simulation presented in Figure 2a. This implies that the largest principal element of the ^{59}Co HFI tensor must be less than 100 MHz. The lack of any resolved fine structure in the CW EPR spectrum necessitated the application of more advanced EPR techniques, ENDOR and ESEEM, to determine the hyperfine coupling parameters.

The Q-band electron spin−echo (ESE) detected EPR spectrum of $\mathbf{1}^+$ (see Figure S1, Supporting Information) is consistent with the CW EPR spectra presented in Figure 2. The Davies ENDOR spectrum collected at 1053.2 mT, on resonance with $g_\perp$, is shown in the top of Figure 3.[36] Two main peaks are observed: one centered at ≈26 MHz and one lesser intense feature centered at 48 MHz. These features are split by approximately twice the Larmor frequency of ^{59}Co (υ_L = 10.5 MHz at 1053.2 mT), which suggest they arise from a hyperfine-coupled cobalt center. An additional data set collected in resonance with the most intense portion of the $g_{||}$ feature (B_0 = 1165 mT; Figure 3, bottom) lacks the highest-frequency component of the $g_\perp$ spectrum. Instead, only a broad feature spanning 10−25 MHz is visible. To simulate these orientation-selected (excitation bandwidth of 50 MHz used in the simulations) ^{59}Co ENDOR spectra, we initially used the ^{59}Co hyperfine interactions predicted by DFT ([e.g., −17, −46, 78] for MOD-$\mathbf{1}^+$xtal, vide infra). These HFI values were then varied over a modest range (±30 MHz) until the positions and line-shapes of features in the experimental spectrum were reproduced. Ultimately, all features are well-simulated with a single class of cobalt ions with $A(^{59}\text{Co})$ = [−20(±2), 77(±2), −5(±15)] MHz (Figure 3, black traces). The largest ^{59}Co hyperfine interaction element is along the $g_\perp$ axes and points to either a $3d_{xz}$ or $3d_{yz}$ orbital as the home of the unpaired spin density on cobalt.[37] Four such cobalt ions were included that differed only in the relative orientation of the A-tensors: two with Euler angles [α, β, γ] of [0, 0, 0]° and two with [90, 0, 0]° relative to g = [2.35, 2.32, and 2.06]. This essentially mimics the D_{2d} symmetry of $\mathbf{1}^+$ where the two cobalt ions have

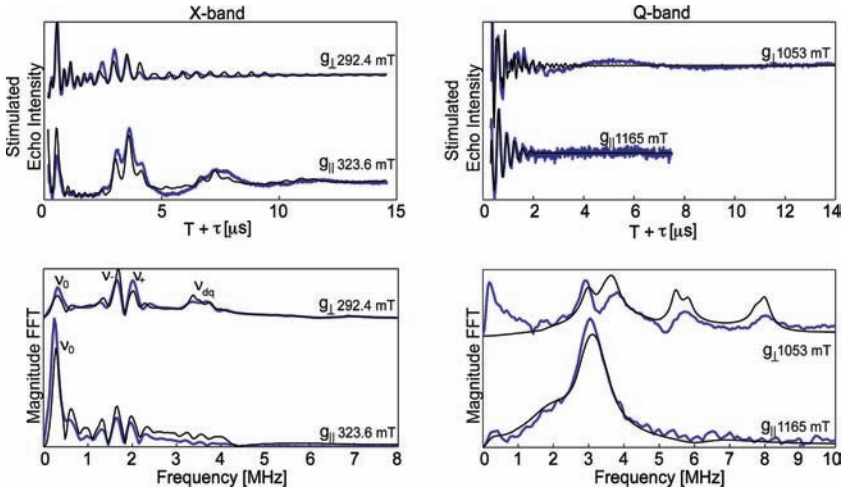

Figure 5. Three-pulse ESEEM spectra of $\mathbf{1}^+$ taken at both perpendicular (282 and 1053 mT) and parallel (324 and 1165 mT) turning points at X- and Q-band frequencies (blue). To simulate, four equivalent nitrogen nuclei with $A(^{14}\mathrm{N}) = [1.31, 1.89, 0.92]$ MHz, $e^2Qq/h = 2.35$ MHz, and $\eta = 0.21$ were used (black). The orientation of two of the nitrogen nuclei was rotated by 90° to mirror the symmetry of $\mathbf{1}^+$. Spectrometer settings: temperature = 10 K. For X-band, $t_{\pi/2} = 20$ ns, $\tau = 144$ ns. For Q-band, $t_{\pi/2} = 40$ ns, $\tau = 300$ ns.

local coordinate frames that are rotated by 90° about the molecular *z*-axis relative to the other two cobalt ions. The rather large range of acceptable values for $A_{||}$ results from the breadth of the ENDOR feature detected in resonance with $g_{||}$. The magnitude of the hyperfine anisotropy is smaller than that typically found for mononuclear Co(IV) systems wherein the unpaired spin is largely localized on a single metal center (cf. Table 1). Such small ^{59}Co HFI values are more commonly found for a species in which there is significant (up to 50%) spin density delocalized onto the ligands.[34]

Mims ENDOR spectroscopy was used to probe the strength of proton HFI in $\mathbf{1}^+$ (Figure 4). The $g_\perp$ spectrum of the fully proteated complex is rather narrow with features centered at the proton Larmor frequency and split by 0.15, 0.30, 0.90, and 1.35 MHz (Figure 4, left panel, top). The spectrum acquired in resonance with $g_{||}$ is slightly wider with features split by 0.70 and 1.75 MHz (Figure 4, left panel). By selectively deuterating the pyridine rings at the *ortho* positions, we observe that the most strongly split features completely disappear (Figure 4, bottom). The difference between these two spectra gives features from solely the *ortho* protons.[38] These difference spectra are well-simulated using a single class of rhombic contribution: $A(^1\mathrm{H}) = [0.45, 1.45, -1.90]$ MHz (Figure 4, black traces). These HFI are purely dipolar in nature, indicating no spin density is found at the proton nucleus. Perdeuteration of the pyridine ligands leads to further narrowing of the ENDOR spectrum (see Figure S7, Supporting Information), and the remaining features must arise from very weak HFI of the methyl-group protons from the four acetate ligands. Weak HFI interactions from the solvent molecules likely also contribute to the observed spectra.

To elucidate the ^{14}N hyperfine couplings, three-pulse ESEEM experiments were performed at both the X-band (at 282 and 324 mT) and Q-band (at 1053 and 1165 mT) in resonance with $g_\perp$ and $g_{||}$, respectively (Figure 5). At the X-band, τ values were chosen to suppress the contribution from the weakly hyperfine-coupled protons. The X-band ESEEM spectrum collected in resonance with $g_\perp$ possesses intense peaks at 0.35, 1.70, 2.05, and 3.40 MHz. The first three of these features are assigned to the transitions between nearly pure quadrupole states (υ_0, υ_-, and υ_+, respectively) and are indicative of a ^{14}N nucleus experiencing near-cancellation conditions, wherein half the magnitude of the hyperfine interaction is approximately equal to the nitrogen Larmor frequency ($A/2 = \upsilon_\mathrm{L}(^{14}\mathrm{N}) = 0.87$ MHz at 282 mT). The fourth strong feature is attributed to the double-quantum (υ_{dq}) transition between the $m_I = \pm 1$ spin levels of the nitrogen nucleus. Notably, the X-band ESEEM spectrum collected in resonance with $g_{||}$ shows only the feature at 0.35 MHz.[39,40] This behavior is expected when the hyperfine-coupled nitrogen is oriented with the axis of the principal value of its nuclear quadrupole interaction (NQI) q_{zz} parallel to the vector of the resonant *g*-value.[39] In this case, it means that the orientation of q_{zz} is coincident with the $g_{||}$ vector (i.e., the Euler angle $Q_\beta \approx 0°$). This is not surprising given the D_{2d} symmetry of the molecule (the principal C_2 axis runs parallel to all four Co−N bonding vectors, Scheme 1). Furthermore, that we see no other strong peaks in this spectrum indicates either that one nitrogen is hyperfine coupled with $A \approx 1.7$ MHz and the remaining three nitrogen nuclei experience a dramatically different amount of unpaired spin density or that all four nitrogens in the complex have identical HFI and NQI parameters. The latter view is supported by the presence of small features in the X-band ESEEM spectrum at 0.75, 1.25, 2.45, ca. 5.5, and ca. 7.0 MHz (collected at 282 mT). These peaks are assigned, respectively, to the following combination bands: $2\upsilon_0$; $3\upsilon_0$ or $\upsilon_- - \upsilon_0$; $\upsilon_+ + \upsilon_0$; $\upsilon_{dq} + \upsilon_0$; and $2\upsilon_{dq}$. Such combination frequencies only manifest in three-pulse ESEEM spectra when multiple nearly equivalent nuclei are present.

The Q-band ESEEM spectrum acquired in resonance with $g_\perp$ has four features centered at 3.0, 4.2, 5.8, and 8.1 MHz. The peak at 8.1 MHz is assigned to υ_{dq}, having shifted to higher frequency by 4.75 MHz (twice the difference in the respective ^{14}N Larmor frequencies) as the magnitude of B_0 was increased from 282 to 1053 mT. The single quantum nuclear spin-flip frequencies in this same electron spin manifold should appear at approximately half the value of υ_{dq}, or 4 MHz, in this case. The remaining two features at 3.0 and 5.8 MHz correspond to the υ_{sq} and υ_{dq} features, respectively, from the opposite electron spin manifold in which the nuclear Zeeman and ^{14}N hyperfine interactions

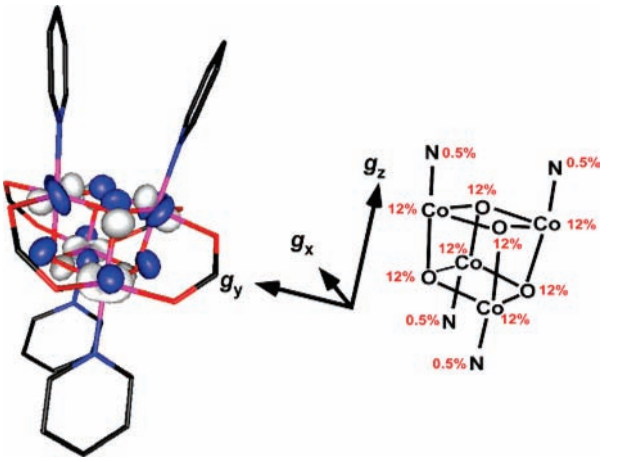

Figure 6. Singly occupied molecular orbitals of $\mathbf{1}^+$ from DFT calculations. Calculations show the unpaired electron spin density spread almost equally over the eight core atoms of the cubane based on their Löwdin spin populations.

oppose one another. The Q-band ESEEM spectrum collected in resonance with $g_{||}$ has only one major feature at 3.2 MHz with a shoulder visible to lower frequency. This is due to the single crystal-like orientation selectivity that is achieved at the $g_{||}$ turning point.

To simulate the data collected at both $g_\perp$ and $g_{||}$, for both frequencies, we first employed a single nitrogen with the magnetic parameters $A(^{14}\mathrm{N}) = [1.31, 1.89, 0.92]$ MHz, a quadrupole coupling $e^2Qq/h = 2.35$ MHz, and $\eta = 0.21$. The best-fit Euler angles for the hyperfine and quadrupole tensors relative to the g-tensor were found to be $[-90, -90, 155]^\circ$ and $[-115, 0, -90]^\circ$, respectively, and are consistent with the observed orientation dependence above. This procedure reproduced the major features evident in the experimental spectrum; however, the sum and difference frequency combination bands described above were absent from the simulation. These combination features only arise by including additional, identical hyperfine-coupled ^{14}N nuclei in the simulation. Mirroring the symmetry of $\mathbf{1}^+$, we ultimately include two sets of two identical nitrogens differing only in that, for one of these sets, the hyperfine and quadrupole tensors are rotated by 90° about the g_z-axis. The inclusion of four nitrogens is also necessary to accurately predict the depth of the envelope modulation (Figure S6, Supporting Information). The smallness of the isotropic portion of the HFI indicates that relatively little unpaired spin density is present on the nitrogen nuclei (≈0.07%). This result compares favorably to the total nitrogen s-orbital spin density predicted from DFT calculations (≈0.088%).[41,42] These NQI parameters are consistent with those of metal-bound pyridines, though little sigma donation to the metal center occurs.[43]

DFT Results. The geometry-optimized structures of both the reduced ($[Co(III)_4O_4]$, MOD-$\mathbf{1}^0$opt) and oxidized ($[Co(III)_3Co(IV)O_4]$, MOD-$\mathbf{1}^+$opt) forms of **1** maintain the approximate D_{2d} symmetry found in the crystal structure (refer to Materials and Methods for computational details). Upon in silico oxidation, some geometric parameters do change (cf. Tables S2 and S3, Supporting Information). Comparing the fully geometry-optimized structures, MOD-$\mathbf{1}^0$opt and MOD-$\mathbf{1}^+$opt, the average Co−N(py) bond length is predicted to increase by 1.8 pm and the Co−O(oxo) bonds *trans* to the pyridine to lengthen by 0.4 pm. Alternatively, the bridging oxos *cis* to pyridine see their bonds to cobalt shrink by 0.3 pm. That these geometrical changes are relatively small and nearly equivalent at all Co centers is due to the electron hole in $\mathbf{1}^+$ being distributed about the cluster, creating four metal centers with some Co(IV) (low-spin d^5) character. This delocalization is illustrated in the isosurface plot of the singly occupied molecular orbital (SOMO), which shows a near equal partitioning of the unpaired electron about the four cobalts and the four μ_3-oxos that compose the cuboidal core, essentially giving $[Co^{+3.125}{}_4O_4]$ (Figure 6). Due to the approximate way in which exchange integrals are computed in DFT, an unnatural Coulombic interaction of an electron with itself contributes to the total energy.[44] This so-called self-interaction error (SIE) can manifest as an artificial delocalization of electron density over the molecule.[45] The use of hybrid functionals—such as PBE0 used here—mitigates this error somewhat. Also, SIE is particularly evident when molecular fragments are separated at long distances which is not the case here as Co−oxo bonds are 1.87 Å long, on average, and the internuclear Co···Co distances are very short, between 2.7 and 2.9 Å.

The predicted g-tensor for both DFT models of $\mathbf{1}^+$, MOD-$\mathbf{1}^+$opt and MOD-$\mathbf{1}^+$xtal, is found to be nearly axial with $g = [2.130, 2.278, 2.280]$ and $[2.175, 2.388, 2.408]$, respectively. Though the computationally determined g-values for MOD-$\mathbf{1}^+$opt are closer to those found experimentally for $\mathbf{1}^+$, the computed hyperfine parameters are in less good agreement (see Discussion below and Tables S4 and S5, Supporting Information). Therefore, we choose to discuss the DFT results for MOD-$\mathbf{1}^+$xtal for the rest of our analysis. However, we note that the differences in computed magnetic properties for MOD-$\mathbf{1}^+$opt and MOD-$\mathbf{1}^+$xtal are relatively small, and our major conclusions are supported equally by both sets of DFT results. The computed ^{59}Co HFI for MOD-$\mathbf{1}^+$xtal are remarkably similar to one another with $A(^{59}\mathrm{Co}) = [-16, -47, 79; -16, -46, 80; -17, -46, 79; -18, -46, 78]$ MHz. ^{59}Co HFI computed using MOD-$\mathbf{1}^+$opt are much more axial with the average $A(^{59}\mathrm{Co}) \approx [-34, -37, 88]$ MHz. Simulation of the CW EPR and ^{59}Co ENDOR data using these parameters and corresponding predicted Euler rotation matrices yields spectra that are in fair agreement with experiment (cf. Figure 3). The rhombicity of the computed HFI is slightly too large to accurately model the feature at 30 MHz in the ENDOR spectrum (Figure S3, Supporting Information). If we instead invoke a single class of the ^{59}Co center and use the HFI determined by our best fit of the ENDOR spectrum along with the Euler rotation matrices predicted by DFT for each of the four hyperfine-coupled cobalt centers, the resultant spectral simulation is in fairly good agreement with experiment. Importantly, the relatively modest strength of the ^{59}Co HFI predicted by DFT and determined from fitting the ^{59}Co ENDOR spectrum can be used to simulate a corresponding CW EPR spectrum (Figure 2). In particular, the $g_{||}$ feature of the CW EPR spectrum is a sensitive reporter of the magnitude of ^{59}Co HFI for the contributing orientations of $\mathbf{1}^+$. We note that the DFT-predicted $A(^{59}\mathrm{Co})$ along the $g_{||}$ axis is too large and leads to too wide an EPR feature at $g = 2.06$ (Figure 2). However, by simply rotating this tensor to allow the largest element of the ^{59}Co HFI to be more along $g_\perp$, the simulated EPR spectrum is in much better agreement with our experimental results, and the predicted orientation dependence of the ^{59}Co ENDOR spectrum is accounted for properly (Figure 3). The cobalt-centered atomic orbitals that contribute to the SOMO presented in Figure 6 each have mostly $3d_{xy}$-character with between 11.7 and 11.8% unpaired spin density (determined

using Löwdin accounting methods), which is consistent with having $g_{\perp} > g_{||} \approx g_e$ (vide infra). Interestingly, the predicted spin density (essentially equivalent to the SOMO, cf. Figure 6 and Supporting Information Figure S4) shows that the equatorial plane of each contributing Co $3d_{xy}$ orbital is canted away from the plane of the "diamond" formed by two cobalt centers and their bridging oxos. The oxo 2p-based in-plane π orbitals are also tilted up from this plane. This orientation allows for overlap with the same atomic orbitals on the opposite face of the cube, illustrating the pathway for spin delocalization over both dimeric halves. We also interpret this canting of the spin-bearing orbitals as supporting our formulation of the magnetic cobalt-based orbital as having significant $d_{xz,yz}$ character.

DFT predicts that the strongest hyperfine-coupled protons will be those located at the *ortho* positions of the pyridine rings, in agreement with our experimental spectra indicated above (cf. traces a and b in Figure 4, top panel). We attempted to model the dipolar contribution to the hyperfine anisotropy of these *ortho*-pyridine protons using a simple eight-point multipole point-dipole approximation where the only variable was the distance between the proton and the eight spin centers, each carrying approximately 1/8 of an unpaired electron. Typically such a calculation yields a dipolar HFI of approximately [0.45, 0.45, −0.90] MHz. This model fails to account for the full magnitude of anisotropy found in the Mims ENDOR spectra (cf. $A_{dip}(^1H_{ortho})$ = [0.45, 1.45, −1.95]) determined by fitting the difference spectra in Figure 4. This points to a breakdown in the point-dipole approximation and suggests that the Co 3d-based magnetic orbital and/or the oxo-bridge p_x- and p_y-orbitals that carry the unpaired electron have lobes that are in close proximity to these protons. Additional unpaired spin density on the pyridine nitrogens (see below) would also contribute to the dipolar HFI of the *ortho*-pyridine protons.

The isotropic ^{14}N HFI predicted by using MOD-$\mathbf{1}^+$xtal (2.05 MHz) is only slightly larger than what we find from fitting the multifrequency ESEEM data in Figure 5 ($A_{iso}(^{14}N)$ =1.37 MHz). The NQI parameters are also in quite good agreement with DFT predicting e^2Qq/h = 2.21 MHz and η = 0.13 compared to e^2Qq/h = 2.35 MHz and η = 0.21 determined above. The spin density on cobalt predicted using MOD-$\mathbf{1}^+$opt is in an orbital that is still best described as d_{xy}, but significant d_{xz} and d_{yz} character is also present, different from that found using MOD-$\mathbf{1}^+$xtal (see Figure S4, Supporting Information). This leads to more direct spin overlap with the nitrogen nucleus (Löwdin spin density of 0.004 versus 0.007) increasing $A_{iso}(^{14}N)$ by 50% from 2.05 to 3.15 MHz. This is also a plausible mechanism for an increase in the anisotropy observed in our ^1H ENDOR above.

On the whole, the relative good agreement between the experimentally determined and DFT-computed magnetic properties validates the electronic structure of $\mathbf{1}^+$ predicted by DFT. Namely, the cuboidal core has a single unpaired electron that is delocalized more-or-less evenly over the four cobalt ions and four bridging oxos. Each of the four metal centers in this $[Co^{+3.125}{}_4O_4]$ cluster has a partial hole in the $3d_{xy}$-based orbital with nonzero $3d_{yz}/d_{xz}$ character that leads to larger ^1H HFI for the *ortho* pyridine protons than would be expected based on a pure eight-point−point dipolar interaction.

DISCUSSION

On the basis of the EPR properties measured for $\mathbf{1}^+$, we conclude that there is but one unpaired electron almost evenly distributed over the eight atoms that compose the core of the cube. Our DFT results on a low-spin, S = 1/2, model for this

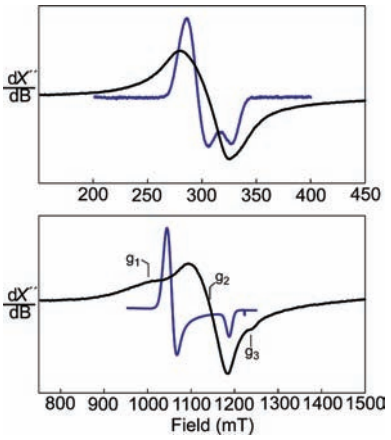

Figure 7. Comparison of $\mathbf{1}^+$ (blue) and the "Co(IV)" signal of Co−Pi (black) at X- and Q-band frequencies (top and bottom, respectively). Spectra of $\mathbf{1}^+$ were taken at 10 K, and those of Co−Pi were taken at 80 K.

$[Co(III)_3Co(IV)O_4]$ cluster support this formulation. Shown in Table 1 are *g*-tensor and hyperfine values for other known Co(IV) species. When compared to other Co(IV) species, we note that the *g*-values of $\mathbf{1}^+$ fall within the range of literature values. This was unexpected: many of these known mononuclear Co(IV) systems have spin densities much greater than 12.5% on the cobalt atoms, yet these systems have very similar or even smaller *g*-shifts relative to $\mathbf{1}^+$. Generally, as the spin is delocalized over more atoms, a smaller deviation from the free-electron *g*-value is expected. This minimization of the *g*-shift is a result of spin density being removed from metal centers that have large spin−orbit coupling constants and spread over a larger subset of atoms with smaller spin−orbit couplings. The orientations of these local *g*-tensors are not necessarily coincident with each other, thus their sum averages out large *g*-shifts.

One possible explanation, to rationalize the contrast between the expected and observed *g*-tensors, assumes four equivalent, hypothetical, cobalt monomers whose interactions sum to give the observed properties of the system.[46] In this arrangement, just under half of the unpaired electron resides on symmetry equivalent—in the D_{2d} point group—cobalt centers. Because of this equivalency, a cobalt tetramer with an eighth of the unpaired spin density on each atom of the core is roughly analogous to a cobalt monomer housing half the spin density. Harmer et al. found similar ^{59}Co hyperfine values for Co(OEC), in which approximately half the unpaired electron spin resides on the cobalt atom and half on the ligand.[34] Christou and co-workers also observe a similar delocalization pattern of the unpaired electron equally over the cobalt atoms in their related cuboidal complex based on the equivalent bond distances for all cobalt ions and the good fit of their anisotropic thermal parameters.[21]

Clearly we show that the unpaired spin in $\mathbf{1}^+$ is distributed in a homogeneous fashion about the whole Co_4O_4 core of this molecule. We see that the high degree of symmetry in $\mathbf{1}^+$ likely causes the site-specific, monomer *g*-axes to be aligned in the Co_4O_4 core of the cube. Due to this effect, delocalization of the unpaired spin density would not average to a net minimization of the *g*-shifts as is often observed. Instead, the aligned *g*-axes allow the site-specific *g*-tensors to add constructively, giving a spectrum more reminiscent of a single cobalt housing 50% of the spin density.

The CW EPR spectra of $\mathbf{1}^+$ and the Co(IV) intermediate of the Co−Pi catalyst are compared in Figure 7. Contributions to

the spectrum of the catalyst from the Co(II) precursor are removed by taking advantage of relatively faster relaxation times of Co(II) when compared to Co(IV): by collecting the EPR spectrum of Co−Pi at 80 K, nearly all of the low-field Co(II) contributions are removed, leaving only the EPR signal arising from the Co(IV) species.[47,48] Upon closer inspection, we see that the resultant spectrum is distinctly different from the spectrum of $\mathbf{1}^+$. While $\mathbf{1}^+$ exhibits an approximately axial g-tensor, the catalyst seems to have more rhombic g-values with g_{eff} = 2.48, 2.19, and 2.01. This difference indicates that the electron configuration for the ground state of Co(IV) species in Co−Pi is different from the formal $(d_{xz},d_{yz},d_{xy})^{5.875}$ arrangement (or equivalently 1/8 of an electron hole in the t_{2g} orbital set) determined in this study for each cobalt center of $\mathbf{1}^+$. Also, there could be low-lying ligand-field excited states that contribute more strongly to the ground-state description of the Co(IV) species in the catalyst film. In other low-spin d^5 systems, this effect has been shown to manifest as larger anisotropy and rhombicity in g-values.[49] Additionally, the broad, non-Gaussian line-shape of the g_1 feature in the Co(IV) Co−Pi spectrum is best modeled as arising from a large unresolved ^{59}Co hyperfine. This is in striking contrast to the modest ^{59}Co HFI (A_{max} = 80 MHz) we measured for $\mathbf{1}^+$ (Figure 3) and indicates that the unpaired electron spin observed in Co−Pi is more localized onto a single cobalt center. This formulation is in agreement with recent proposals for the mechanism of water oxidation catalyzed by Co−Pi,[8] where it is postulated that $Co^{3+/4+}$ redox transformations in the film are coupled to proton loss from bound OH ligands. The increase in ligand-field strength accompanying this proton loss may be expected to localize the unpaired spin density. This localization of the oxidized equivalent is consistent with subsequent reactivity of the Co(IV) moieties. In the catalyst film, it is believed that terminal and bridging Co(IV)-oxos couple to form the O−O bond and release molecular oxygen.[8] In contrast, the oxidizing prowess of $\mathbf{1}^0$ is limited to substrates such as alcohols (to ketones) in the presence of alkylperoxides.[50] Thus far, $\mathbf{1}^0$ and $\mathbf{1}^+$ have not been shown to be capable of generating the multiple Co(IV) moieties needed to do water oxidation electrochemically. These findings suggest that hole localization, through the coupling of proton and electron, may be requisite for efficient oxygen evolution in the Co−Pi catalyst film. However, it was very recently reported that $\mathbf{1}^0$, in the presence of $Ru(bpy)_3$ and $Na_2S_2O_8$, can photooxidize water.[51] If substrate water binding were to take place and break the high degree of molecular symmetry, subsequent changes in the ligand-field strength due to water/hydroxide proton loss could be great enough to cause a localization of the unpaired spin density. If however the complex opens to release molecular oxygen from the cubane's core oxo groups, electronic structure changes are much more difficult to predict.

■ ASSOCIATED CONTENT

Supporting Information. Cartesian coordinates for models used in DFT calculations. Spectral simulations using MOD-$\mathbf{1}^+$opt DFT results. Spin densities and magnetic parameters computed using DFT. This material is available free of charge via the Internet at http://pubs.acs.org.

■ AUTHOR INFORMATION

Corresponding Author
rdbritt@ucdavis.edu

Present Addresses
[‖]Present address: Department of Chemistry, Room 419 Latimer Hall, University of California, Berkeley, CA 94720.

■ ACKNOWLEDGMENT

Support for this research came from the National Science Foundation via grant CHE-0939178 (to R.D.B) and EAR-0814242 (to W.H.C.), from the U.S. Department of Energy Office of Basic Energy Science via grant numbers DE-FG03-96ER-14629 and DE-FG03-02ER-15693 (to W.H.C.) and AFOSR FA 9950-09-1-0689 (to D.G.N.). Y.S. gratefully acknowledges the National Science Foundation for a predoctoral fellowship.

■ REFERENCES

(1) Kanan, M. W.; Nocera, D. G. *Science* **2008**, *321*, 1072.
(2) Kanan, M. W.; Surendranath, Y.; Nocera, D. G. *Chem. Soc. Rev.* **2009**, *38*, 109.
(3) Lutterman, D. A.; Surendranath, Y.; Nocera, D. G. *J. Am. Chem. Soc.* **2009**, *131*, 3838.
(4) Esswein, A. J.; Surendranath, Y.; Reece, S. Y.; Nocera, D. G. *Energy Environ. Sci.* **2011**, *4*, 499.
(5) Surendranath, Y.; Dincă, M.; Nocera, D. G. *J. Am. Chem. Soc.* **2009**, *131*, 2615.
(6) Lewis, N. S.; Nocera, D. G. *Proc. Natl. Acad. Sci. U.S.A.* **2006**, *103*, 15729.
(7) Casey, W. H. *J. Colloid Interface Sci.* **1991**, *146*, 586.
(8) Surendranath, Y.; Kanan, M. W.; Nocera, D. G. *J. Am. Chem. Soc.* **2010**, *132*, 16501.
(9) Risch, M.; Khare, V.; Zaharieva, I.; Gerencser, L.; Chernev, P.; Dau, H. *J. Am. Chem. Soc.* **2009**, *131*, 6936.
(10) Kanan, M. W.; Yano, J.; Surendranath, Y.; Dincă, M.; Yachandra, V. K.; Nocera, D. G. *J. Am. Chem. Soc.* **2010**, *132*, 13692.
(11) Gerken, J. B.; McAlpin, J. G.; Chen, J. Y. C.; Rigsby, M. L.; Casey, W. H.; Britt, R. D.; Stahl, S. S. *J. Am. Chem. Soc.* **2011**, DOI: 10.1021/ja205647m.
(12) McAlpin, J. G.; Surendranath, Y.; Dincă, M.; Stich, T. A.; Stoian, S. A.; Casey, W. H.; Nocera, D. G.; Britt, R. D. *J. Am. Chem. Soc.* **2010**, *132*, 6882.
(13) Buffat, B.; Demazeau, G.; Pouchard, M.; Dance, J. M.; Hagenmuller, P. *J. Solid State Chem.* **1983**, *50*, 33.
(14) Motohashi, T.; Ono, T.; Sugimoto, Y.; Masubuchi, Y.; Kikkawa, S.; Kanno, R.; Karppinen, M.; Yamauchi, H. *Phys. Rev. B* **2009**, *80*, 165114.
(15) Motohashi, T.; Ono, T.; Katsumata, Y.; Kanno, R.; Karippinen, M.; Yamauchi, H. *J. Appl. Phys.* **2008**, *103*, 07C902.
(16) Hertz, J. T.; Huang, Q.; McQueen, T.; Klimczuk, T.; Bos, J. W. G.; Viciu, L.; Cava, R. J. *Phys. Rev. B* **2008**, *77*, 075119.
(17) Kawasaki, S.; Motohashi, T.; Shimada, K.; Ono, T.; Kanno, R.; Karppinen, M.; Yamauchi, H.; Zheng, G. *Phys. Rev. B* **2009**, *79*, 220514.
(18) Townsend, M. G.; Hill, O. F. *Trans. Faraday Soc.* **1965**, *61*, 2597.
(19) Vanzee, R. J.; Hamrick, Y. M.; Li, S.; Weltner, W. *J. Phys. Chem.* **1992**, *96*, 7247.
(20) Warda, S. A.; Massa, W.; Reinen, D.; Hu, Z. W.; Kaindl, G.; de Groot, F. M. F. *J. Solid State Chem.* **1999**, *146*, 79.
(21) Dimitrou, K.; Brown, A. D.; Concolino, T. E.; Rheingold, A. L.; Christou, G. *Chem. Commun.* **2001**, 1284.
(22) Symes, M. D.; Surendranath, Y.; Lutterman, D. A.; Nocera, D. G. *J. Am. Chem. Soc.* **2011**, *133*, 5174.
(23) Chakrabarty, R.; Bora, S. J.; Das, B. K. *Inorg. Chem.* **2007**, *46*, 9450.
(24) Calvo, R.; Abresch, E. C.; Bittl, R.; Feher, G.; Hofbauer, W.; Isaacson, R. A.; Lubitz, W.; Okamura, M. Y.; Paddock, M. L. *J. Am. Chem. Soc.* **2000**, *122*, 7327.
(25) Sienkiewicz, A.; Smith, B. G.; Veselov, A.; Scholes, C. P. *Rev. Sci. Instrum.* **1996**, *67*, 2134.

(26) Stoll, S.; Britt, R. D. *Phys. Chem. Chem. Phys.* **2009**, *11*, 6614.
(27) Stoll, S.; Schweiger, A. *J. Magn. Reson.* **2006**, *178*, 42.
(28) Neese, F. *ORCA - an ab initio, Density Functional and Semi-empirical Program Package*, version 2.6, 2008 ed.; Universitat Bonn: Bonn, Germany, 2007.
(29) Perdew, J. P.; Burke, K.; Ernzerhof, M. *Phys. Rev. Lett.* **1996**, *77*, 3865.
(30) Schafer, A.; Horn, H.; Ahlrichs, R. *J. Chem. Phys.* **1992**, *97*, 2571.
(31) Neese, F. *J. Chem. Phys.* **2001**, *115*, 11080.
(32) Laaksonen, L. *gOpenMol 2.32*; Center for Scientific Computing: Espoo, Finland, 2002.
(33) Pfaff, F. F.; Kundu, S.; Risch, M.; Pandian, S.; Heims, F.; Pryjomska-Ray, I.; Haack, P.; Metzinger, R.; Bill, E.; Dau, H.; Comba, P.; Ray, K. *Angew. Chem., Int. Ed.* **2011**, *50*, 1711.
(34) Harmer, J.; Van Doorslaer, S.; Gromov, I.; Broring, M.; Jeschke, G.; Schweiger, A. *J. Phys. Chem. B* **2002**, *106*, 2801.
(35) Adamian, V. A.; Dsouza, F.; Licoccia, S.; Divona, M. L.; Tassoni, E.; Paolesse, R.; Boschi, T.; Kadish, K. M. *Inorg. Chem.* **1995**, *34*, 532.
(36) Additional Davies ENDOR spectra were collected at the low-field extreme of the EPR envelope to guarantee orientation selection of only the perpendicular turning point features. The resulting spectrum was essentially identical to that presented in Figure 3 (top) with only a difference in the signal-to-noise ratio (data not shown).
(37) Here we assume that the $A(^{59}\mathrm{Co})$ z-axis lies along the $g_{||}$ axis of the molecule.
(38) The difference spectrum was computed by scaling the 1+ spectrum relative to 1+ d2-py until the subtracted spectrum possessed only positive features.
(39) Flanagan, H. L.; Singel, D. J. *J. Chem. Phys.* **1987**, *87*, 5606.
(40) Flanagan, H. L.; Singel, D. J. *Chem. Phys. Lett.* **1987**, *137*, 391.
(41) These values were calculated assuming an s-orbital hyperfine value of 1811 MHz at 100% spin population. See Morton and Preston reference.[34]
(42) Morton, J. R.; Preston, K. F. *J. Magn. Reson.* **1978**, *30*, 577.
(43) Rubenacker, G. V.; Brown, T. L. *Inorg. Chem.* **1980**, *19*, 392.
(44) Neese, F. *Coord. Chem. Rev.* **2009**, *253*, 526.
(45) Lundberg, M.; Siegbahn, P. E. M. *J. Chem. Phys.* **2005**, 122.
(46) Neese, F.; Zumft, W. G.; Antholine, W. E.; Kroneck, P. M. H. *J. Am. Chem. Soc.* **1996**, *118*, 8692.
(47) Marts, A.; Greer, S.; Whitehead, D.; Woodruff, T.; Breece, R.; Shim, S.; Oseback, S.; Papish, E.; Jacobsen, F.; Cohen, S.; Tierney, D. *Appl. Magn. Reson.* **2011**, *40*, 501.
(48) Jenkins, D. M.; Di Bilio, A. J.; Allen, M. J.; Betley, T. A.; Peters, J. C. *J. Am. Chem. Soc.* **2002**, *124*, 15336.
(49) Raitsimring, A. M.; Borbat, P.; Shokhireva, T. K.; Walker, F. A. *J. Phys. Chem.* **1996**, *100*, 5235.
(50) Chakrabarty, R.; Sarmah, P.; Saha, B.; Chakravorty, S.; Das, B. K. *Inorg. Chem.* **2009**, *48*, 6371.
(51) McCool, N. S.; Robinson, D. M.; Sheats, J. E.; Dismukes, G. C. *J. Am. Chem. Soc.* **2011**, *133*, 11446.
(52) Webster, R. D.; Heath, G. A.; Bond, A. M. *J. Chem. Soc., Dalton Trans.* **2001**, 3189.
(53) Collins, T. J.; Powell, R. D.; Slebodnick, C.; Uffelman, E. S. *J. Am. Chem. Soc.* **1991**, *113*, 8419.
(54) Halpern, J.; Topich, J.; Zamaraev, K. I. *Inorg. Chim. Acta* **1976**, *20*, L21.
(55) Topich, J.; Halpern, J. *Inorg. Chem.* **1979**, *18*, 1339.
(56) Nikitaeva, G. A.; Nikitaev, A. T.; Zamaraev, K. I.; Sigan, A. L.; Levitin, I. Y.; Volpin, M. E. *J. Struct. Chem.* **1978**, *19*, 243.